



ORIGINAL RESEARCH ARTICLE

Numerical Optimization and Performance Study of Ni-Based Coatings on Gray Cast Iron Surface by High-Speed Laser Cladding Based on Orthogonal Test

Huan Li, Muhua Mao, Rui Wang, Runze Wei, Chunjiang Zhao, Changyao Ouyang, Rui Deng, and Qiaofeng Bai

Submitted: 13 December 2023 / Revised: 22 February 2024 / Accepted: 21 March 2024

To improve the cladding quality of Ni-based powder on gray cast iron by high-speed laser cladding, ANSYS was used to construct the cladding model. The effects of laser power P , scanning rate v , and spot diameter r on the cladding quality were explored in terms of substrate surface temperature, temperature gradient G /solidification rate R , and heat-affected zone (HAZ) by the three-factor and three-level orthogonal test. The parameters that significantly affect the factors v and r were determined. Based on simulation tests, the effect of P on the microstructure, hardness and wear resistance of the molten layer was investigated by using scanning electron microscopy (SEM), hardness tester, friction wear machine and ultra-depth of field. The results showed that the microstructure of the cladding layer became sparse and coarse with increasing P , and the cross-sectional hardness and surface hardness didn't change much. Compared to 2000 W, the wear quality loss of 1600 and 2400 W is improved by 24.8, 40.4%. The best wear resistance was achieved for 2000 W. The wear resistance and bond strength of Ni-based coating are optimal when $v = 3$ mm, $r = 30$ mm/s, and $P = 2000$ W.

Keywords gray cast iron, high-speed laser cladding, microstructure, orthogonal test, wear resistance

1. Introduction

Cast iron has better strength and cost effectiveness (Ref 1), and was widely used for components with certain demand for volume and load-bearing capacity, such as engine blocks, machine tools, and other important castings (Ref 2). This type of gray iron parts have a short service life and high replacement cost, and surface repair modification techniques such as overlay welding and brush plating are usually used to repair the surface defects of these parts and improve their wear and corrosion resistance (Ref 3-5). Laser cladding as an emerging surface modification technology with excellent cladding quality and little heat-affected zone can satisfy the repair needs of different parts (Ref 6, 7). Gray cast iron contains more brittle oxides (Ref 2) and was prone to cracking by laser impact, which can be improved the quality of laser cladding by optimizing process parameters, regulating dilution rate and microstructure.

Huan Li, Runze Wei, Chunjiang Zhao, Changyao Ouyang, Rui Deng, and Qiaofeng Bai, School of Mechanical Engineering, Taiyuan University of Science and Technology, Taiyuan 030024, China; Muhua Mao, Ertuoqianqi Great Wall No. 5 Mining Co., Ltd., Ertokqianqi 016200, China; and Rui Wang, School of Mechanical Engineering, Taiyuan University of Science and Technology, Taiyuan 030024, China; and School of Mechanical and Equipment Engineering, Hebei University of Engineering, Handan 056038, China. Contact e-mail: zhaochunjiang75@163.com.

Zhu et al. (Ref 8) showed that they prepared a Cu-Ti-Ni composite coating on the surface of gray cast iron by laser cladding system, and the coating could significantly improve the performance of the substrate under severe service conditions. Ding et al. (Ref 9) produced a composite coating using titanium powder on gray cast iron with laser cladding. The results show that the average microhardness of the coating rose up by more than three times compared to the substrate material, and the coating exhibited good wear resistance. Kiehl et al. (Ref 10) investigated and examined the corrosion properties of Stellite™ 6 coatings on gray cast iron. The results showed that coatings have a pronounced corrosion resistance compared to gray cast iron.

Laser cladding is a transient non-equilibrium dynamic melting and cooling solidification process, while the melting of the substrate and powder will lead to changes in the dilution rate (Ref 11). In the ideal condition the depth of the melt pool on the substrate surface was shallow to ensure better metallurgical bonding between the clad layer and the substrate on the one side and the mechanical properties and corrosion resistance of the clad layer on the other side (Ref 12). Tian et al. (Ref 13) constructed a laser cladding heat transferring and flowing model from which it was found that the melt pool geometry, dilution rate and relative energy to mass ratio were correlated. Yi et al. (Ref 14) showed that as the v increased, the diffusion of carbon atoms in gray cast iron intensified and refined, inhibiting undesirable defects and crack sprouting, and that the P had less effect on the graphite structure. Huang et al. (Ref 15) found that by increasing v , the microstructure became dense and fine, the grain boundary area increased, and the resistance to deformation and the hardness of the clad layer increased. Goodarzi et al. (Ref 16) investigated the effect of process parameters on the melting area of the substrate and the shape of the substrate melt pool, and the results showed that the powder feeding rate has a

large effect on the shape of the melting area, and increasing P caused an increase in the melting volume of the substrate.

The microstructure and grains of the cladding layer are influenced by the thermal history, while the grain shape, size and growth direction affect the properties of the cladding layer. During solidification of the molten layer, G/R is an important judge of the columnar-isometric transition (G is the temperature gradient and R is the solidification rate), with higher ratios being columnar crystals and lower ratios being fine isometric crystals (Ref 17). Ma et al. (Ref 18) used a three-dimensional finite element model to predict the solidification process of laser clad 316L and found that the average size of grains in the melt pool increased as the P increased. Liu et al. (Ref 19) studied the temperature variation from the top of the molten layer to the surface of the substrate and showed that increasing P and v can increase G . Bai et al. (Ref 20) found that the grains grow along the cladding direction, and as the cladding height increases, G/R gradually decreases, planar crystals transform to cytosol crystals, and coarse columnar crystals begin to grow.

In this paper, a three-dimensional simulation model for high-speed laser cladding of Ni-based coatings on gray cast iron was established, and the influence of process parameters (P , v , r) on the cladding quality was explored by orthogonal tests. The influence of process parameters on the quality of fusion cladding was comprehensively analyzed by three aspects, including the substrate surface temperature, G/R , and the depth of phase change in HAZ (PTZ). From the simulation results, significant factor combinations were selected for the actual fusion cladding experiments. Only a single process parameter with less influence was varied for cladding the Ni-based coatings, and its microstructure, hardness, and wear resistance were analyzed.

2. Material and Experiment

The substrate material is gray cast iron, the fused powder is Ni-based, and the elemental composition is shown in Table 1. In addition gray cast iron contains less S (0.02 wt.%), Mg (0.035 wt.%). Simulation modeling and analysis using ANSYS software. The specific process of the experiment is shown in Fig. 1.

The substrate size is 100 mm × 100 mm × 15 mm, and the substrate surface was polished by milling machine and wiped clean with anhydrous ethanol, and then dried naturally for laser cladding. Six degrees of freedom displacement using a KUKA robotic arm gripping an RFL-C4000 (Raycus Fiber Laser, Wuhan, China) high power fiber laser. The laser has a rated power of 4000 W and a wavelength of 1080 ± 5 nm. The Experimental parameters for laser cladding are: r of 3 mm, v of 30 mm/s, overlap rate of 66.7%, and P of 1600, 2000, 2400 W. The powder feeder is a DPSF2 type powder feeder (Dual Package System Framework, Shanghai, China) and powder

Table 1 Main elemental composition of substrate and coating materials (wt.%)

	C	Mn	B	Cr	Si	Cu	Fe	Ni
Substrate	3.3	0.28	3.5	0.1	Bal.	...
Ni-based	0.08	...	1.36	1.42	2.42	...	0.20	Bal.

feeding speed of 1 r/min. The protection and powder feed gas are argon.

The coating surface was sanded by 240-2000 grit sandpaper step by step, polished by metallographic polishing machine and put into ultrasonic cleaning for 10 min, and the surface moisture was wiped by using dust-free cloth. The sample microstructure was observed by using a field emission scanning electron microscope SEM (JSM-7001F, Japan Electronics). The coating cross-sectional microhardness tests were performed by using a Vickers hardness tester (HXD-1000TM, Shanghai, China) with an applied load of 200 g. The coating surface hardness tests were performed by using a Rockwell hardness tester (GR-150 M, Shanghai, China) with a reading range of 20-70 HRC.

Dry friction wear tests were performed on coating experiments with different powers by a multifunctional friction wear tester (CFT-I, ZhongkeKaihua, Lanzhou, China) and the size of the abrasion marks were measured. The surface was weighed twice before and after the wear, and the friction wear test was fixed by using a fixture. The friction substrate is a 5 mm diameter Si₃N₄ ceramic ball with a load of 30 N, a stroke of 10 mm/r, a speed of 500 r/min and a time of 60 min. The mass of the sample before and after the friction test was recorded using an electronic analytical balance. Observe the shape of the abrasion marks through the Keenes VHX-2000 ultra-depth of field.

3. Finite Element Simulation

3.1 Model Building and Simulation Planning

The thermophysical properties such as density, thermal expansion coefficient, Young's modulus, thermal conductivity, poisson's ratio, and specific heat of the substrate and Ni-based coating were obtained by JMatPro software (in Fig. 2). And the above parameters were imported into ANSYS software for simulation. The scanning path and dimensions of this simulation test are shown in Fig. 3(a), with a lap rate of 66.7%, an initial temperature of 22 °C (ambient temperature), and a nickel-based powder absorption rate A_{Ni} of 0.28 (Ref 10). To ensure the reliability and accuracy of the finite element simulation, the single-layer multi-lane simulation model was constructed with actual experimental dimensions of the cladding layer. As shown in Fig. 3(b), the actual SEM measurements at 2400 W, 0.03 m/s and 3 mm parameters resulted in a melt height of 0.75 mm and a melt width of 4.402 mm, which were used as the simulation model cladding layer height and width dimensions.

The APDL language of ANSYS software has been used to prepare the heat source movement program. The cladding process was performed using the raw and dead cell method for the cladding block, and the multi-pass cladding lap is shown in Fig. 3(c). The mesh division is shown in Fig. 3(d), all mesh sizes are 0.3 mm, and the substrate below the cladding layer is fine-meshed using offset factors. Each cladding layer is divided into 10 blocks. Each block is 3 mm in length, the total of 30 blocks, based on the tetrahedral method for meshing. According to the orthogonal experimental method, the control variables were subjected to a three-factor level crossover test, and the experimental parameters of the nine groups are shown in Table 2.

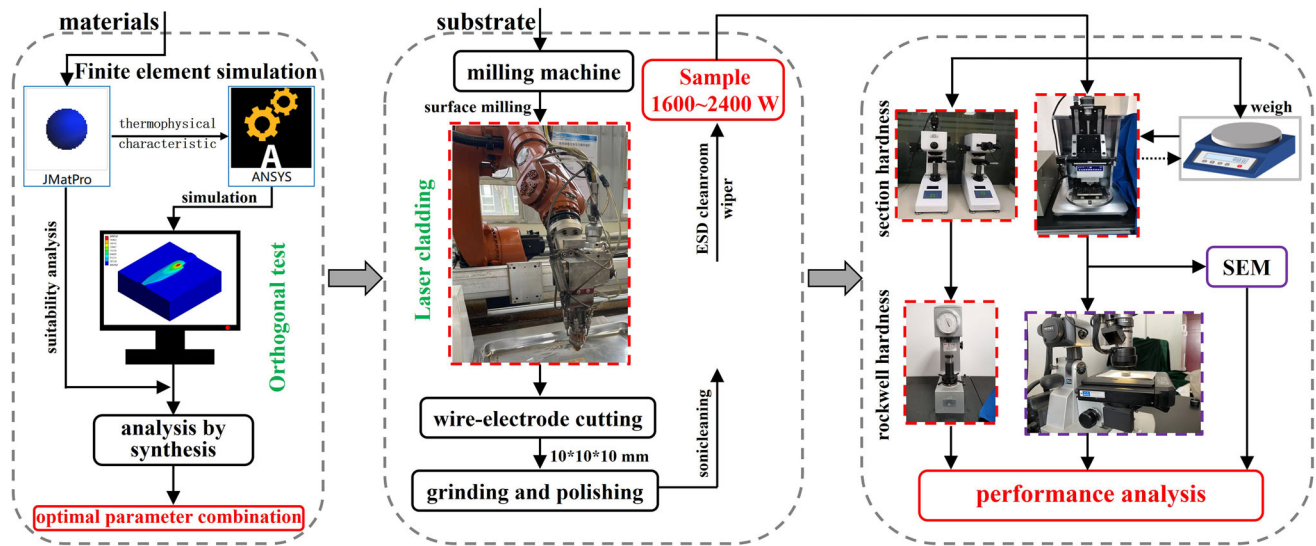


Fig. 1 Experimental process

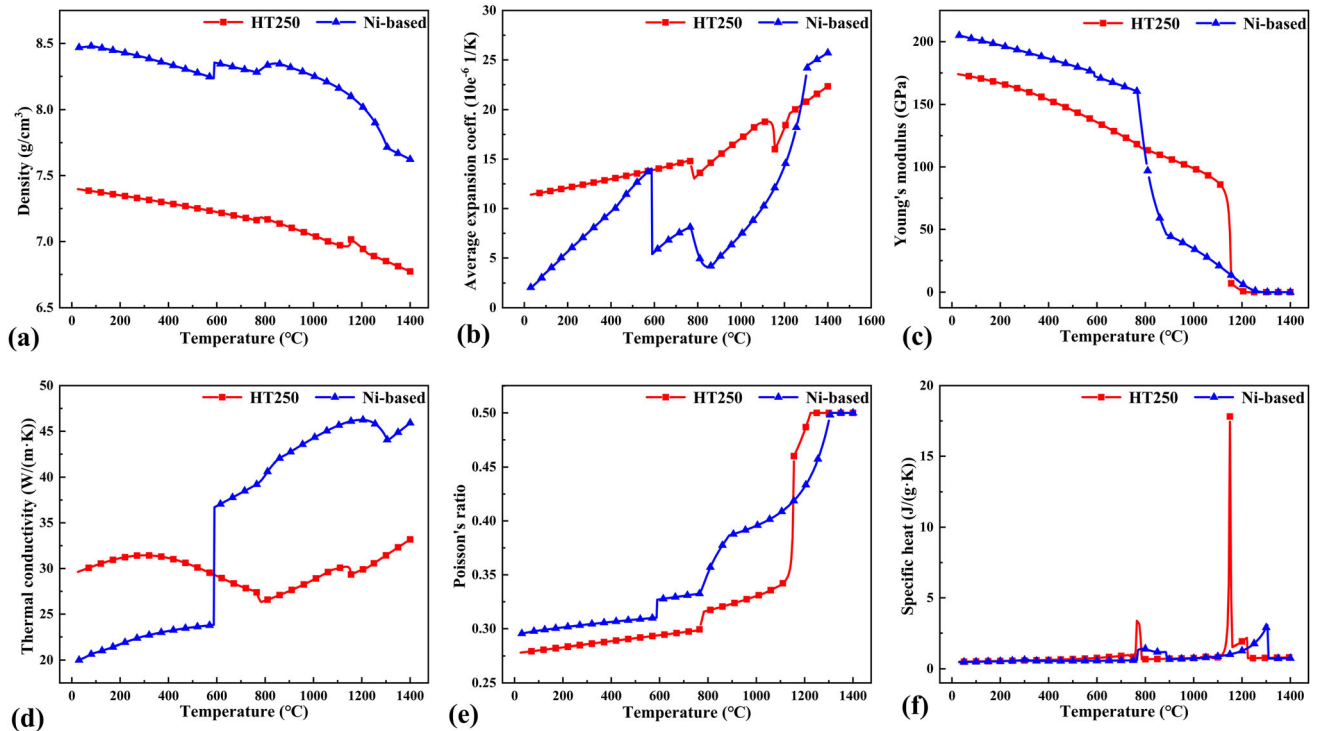


Fig. 2 Thermophysical properties of the substrate and coatings

In transient thermal conduction analysis, the real-time temperature field of the material is a composite function of time and space coordinates with nonlinear heat transfer. The partial differential governing equations for transient heat transfer in anisotropic and isotropic materials are shown in Eq 1 and 2 (Ref 21):

$$\begin{aligned}
 \rho(T)C_p(T) \frac{\partial T}{\partial t} &= \{L\}^T \{ [D] \{L\} T \} + Q \\
 &= \frac{\partial}{\partial x} \left(K_x(T) \frac{\partial T}{\partial x} \right) + \frac{\partial}{\partial y} \left(K_y(T) \frac{\partial T}{\partial y} \right) \\
 &\quad + \frac{\partial}{\partial z} \left(K_z(T) \frac{\partial T}{\partial z} \right)
 \end{aligned}
 \tag{Eq 1}$$

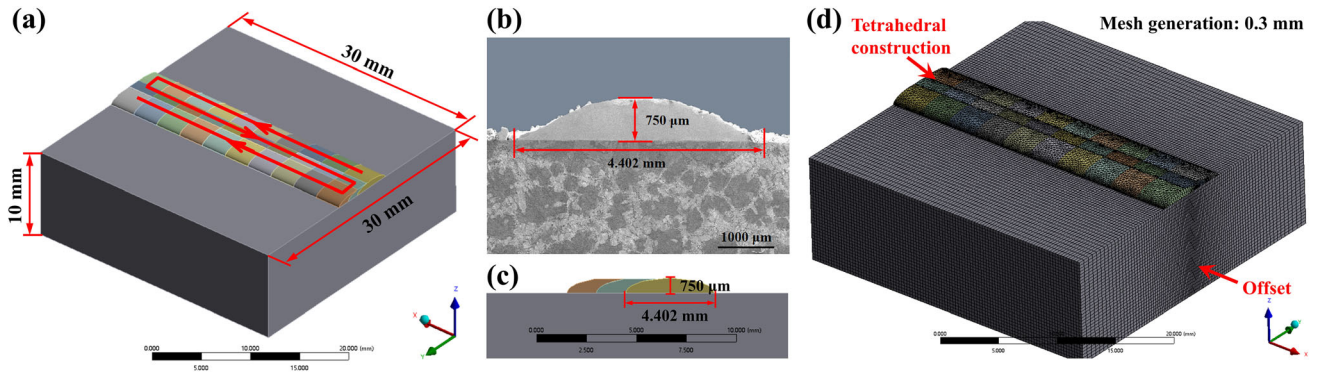


Fig. 3 (a) Scanning path and model dimensions; cladding layer dimensions: (b) experiment, (c) simulation; (d) mesh generation

Table 2 Design of simulation experiment

Group no.	P, W	$v, \text{mm/s}$	r, mm
1	2400	45	4
2	2400	30	3
3	2400	15	2
4	2000	45	3
5	2000	30	2
6	2000	15	4
7	1600	45	2
8	1600	30	4
9	1600	15	3

$$\rho(T)C_p(T) \frac{\partial T}{\partial t} = K(T) \left(\frac{\partial^2 T}{\partial x^2} + \frac{\partial^2 T}{\partial y^2} + \frac{\partial^2 T}{\partial z^2} \right) + Q(x+y+z) \quad (\text{Eq 2})$$

where T is the temperature; t is the heating time; Q is the thermal capacity; $\rho(T)$ is the density with temperature; C_p is the specific heat; $K(T)$ is the thermal conductivity with temperature; $\{L\}$ is the coefficient matrix; $[D]$ is the differential matrix; $\{L\}^T$ is the transverse matrix.

In laser cladding the substrate and coating are heated by the laser to produce radiation and natural convection, this category belongs to the third category of boundary conditions. The boundary condition equations for the HAZ inside and outside the laser beam irradiation region are shown in Eq 3 and 4 (Ref 13):

$$-K(\nabla Tn)|_s = Q - h_f(T - T_0) - \sigma\varepsilon(T_4 - T_0^4) \quad (\text{Eq 3})$$

$$-K(\nabla Tn)|_s = -h_f(T - T_0) - \varepsilon\sigma(T_4 - T_0^4) \quad (\text{Eq 4})$$

where h_f is the thermal convection coefficient; σ is the radiation coefficient $0 \sim 1$; ε is the thermal Boltzmann constant.

In this paper, a RFL-C4000 high-power fiber laser with photoelectric conversion efficiency higher than 25% is used, whose laser source conforms to the Gaussian heat source distribution; the laser mode is that of TEM00; and the heat input is that of a body heat source. The heat source expression is shown in Eq 5 (Ref 22):

$$Q(x, y, z, t) = \frac{2AP}{\eta\pi r^2} \exp\left(-2 \frac{(x-vt)^2 + y^2}{r^2}\right) \exp\left(-\frac{|z|}{\eta}\right) \quad (\text{Eq 5})$$

where A is the laser absorption rate of the alloy powder; P is laser power; r is effective spot diameter; v is scanning rate; η is the optical penetration depth of the powder bed to the incident laser.

The simulated cladding process assumes that: P is constant without fluctuation from external environmental disturbance; the refraction and reflection of the laser by the powder and substrate are not considered; thermal dissipation from high temperature evaporation of metal and liquid metal flow is not considered; the influence of the environment on the escape of laser energy is not considered; influence of the coating-substrate metallurgical interface on thermophysical properties is not considered; all materials are isotropic.

3.2 Temperature Field

This simulation lap form is shown in Fig. 3(c), X -axis is the scanning direction of laser cladding, Y -axis is the lap direction of the cladding layer, Z -axis is the vertical cladding layer and substrate direction, the cladding process is shown in Fig. 4. The single-layer single-pass cladding length was 30 mm, and the total laser cladding length was 90 mm for 2 s, 3 s, and 6 s. The nine experimental groups in Fig. 5a showed similar trends in the increase of the substrate surface temperature, with the fastest temperature increase in Groups 3 and 5. The temperature increases sharply at the beginning of the first and second cladding, and then decreases significantly after the temperature was raised at the third cladding. The first cladding has the fastest temperature increase and less fluctuation, the third cladding has less temperature increase, and the decreasing trend increases after the increase.

Figure 5(a) and (b) show the temperature distribution of the simulation process. In Fig. 5(a) the average temperature (T) of the substrate surface in Groups 1-9 was 480.6, 831.4, 1768.5, 577.6, 1068.0, 705.4, 674.5, 410.6, and 804.2 °C. The maximum temperatures of each group in Fig. 5(b) show the same trend as the average temperature. As calculated in JMatPro, the substrate melting temperature is between 1035 and 1150 °C (in Fig. 5c). Less substrate melting may cause the

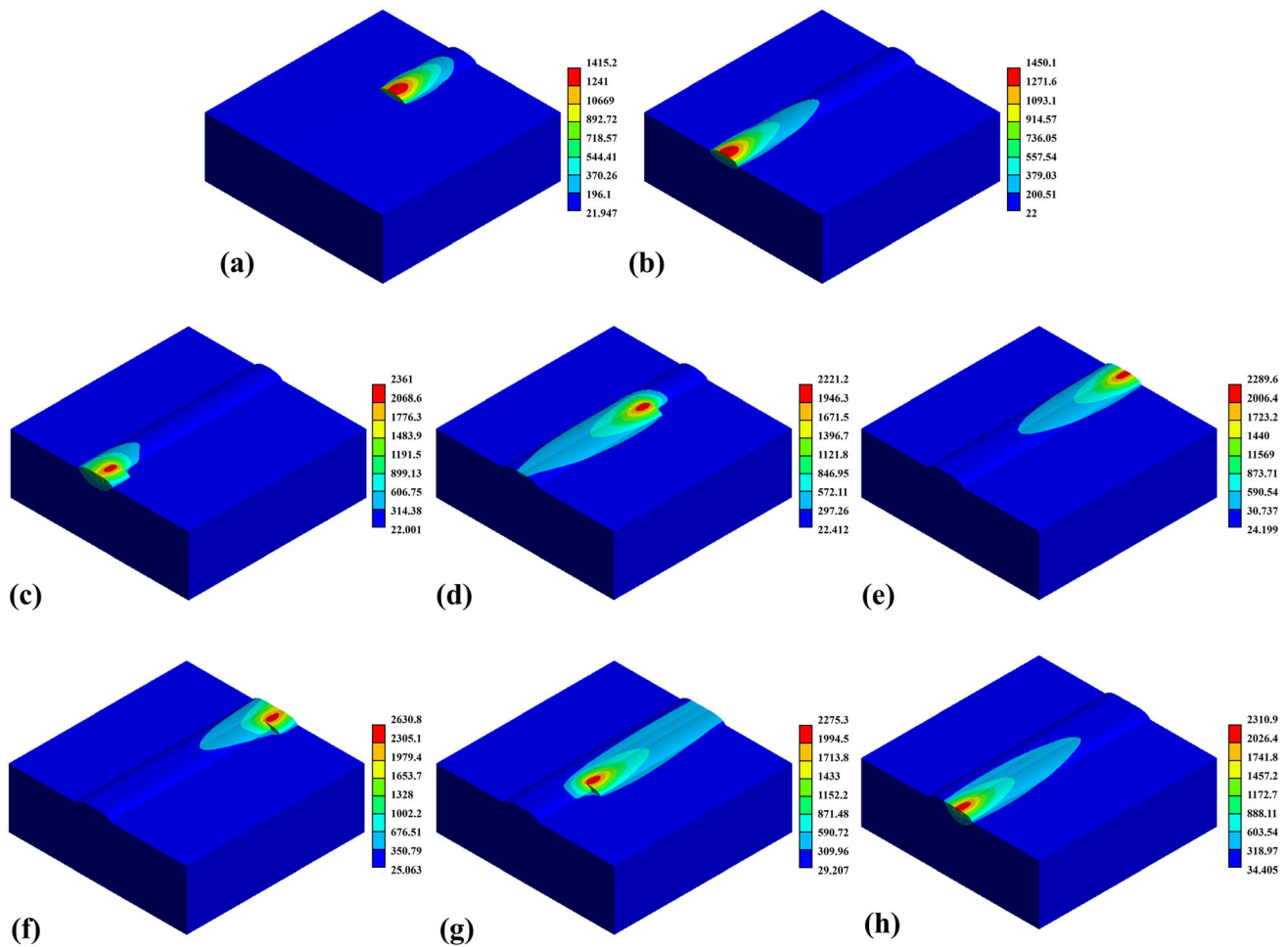


Fig. 4 Temperature field of laser cladding: (a–b) first; (c–e) second; (f–h) third

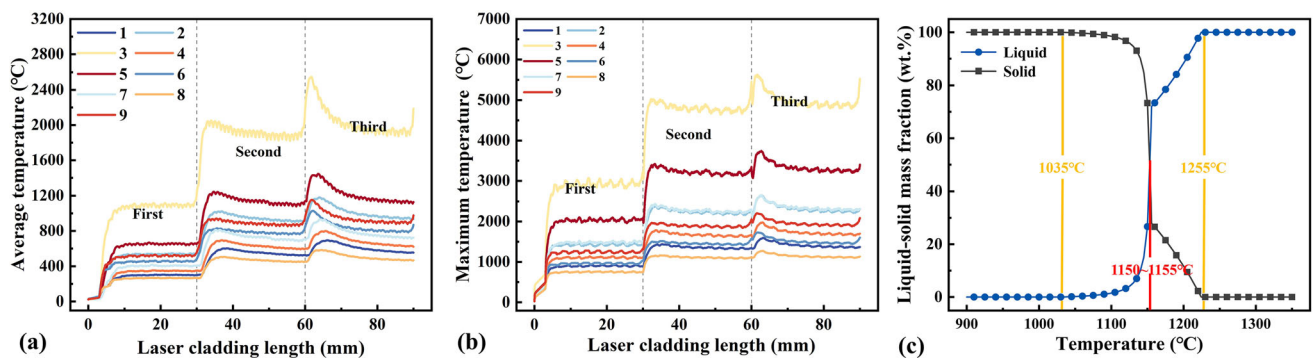


Fig. 5 Substrate surface temperature: (a) average, (b) maximum; (c) melting curve of gray cast iron

metallurgical bond strength to deteriorate and the coating to be easily stripped (Ref 23). Cheng et al. (Ref 24) found that higher laser energy densities and heat inputs increase the substrate's residual stresses, ultimately leading to crack initiation, formation, and expansion.

In conclusion, the heat input of groups 1, 6, and 8 ($r = 4$ mm or $v = 45$ mm/s) is too small, and the metallurgical bonding may be poor. Groups 3 and 5 ($r = 2$ mm or $v = 15$ mm/s) have too much heat input and higher crack sensitivity. Therefore, the energy density input should be within

the appropriate range to ensure good metallurgical bonding and that the substrate is free from cracking and warping.

3.3 G/R

The G is an important influencing factor for microscopic grain formation during laser cladding, and the ratio of G to R is the basis for judging the interconversion of columnar and equiaxed crystals (Ref 17). The grain shape and growth direction affect the cladding layer properties, which is important for the study of the cladding layer tissue formation

mechanism and solidification process. The transformation criteria for columnar and isometric crystals is shown in Eq 6 (Ref 18):

$$G/R = \frac{q/K}{v \cos \alpha} \begin{cases} > C_{st} & \text{Columnar crystal} \\ < C_{st} & \text{Isometric crystal} \end{cases} \quad (\text{Eq 6})$$

where q is the heat flow density; α is the angle between v and R ; C_{st} is the columnar-isometric crystal transition criterion. R is determined by v and the shape of the melt pool, and when $\alpha = 0$, R is the maximum solidification rate, and its value is the same as v . Ma et al. (Ref 18) found that R is maximum in the center of the melt pool and minimum at the edge of the pool, and that the solidification and cooling rates were similarly distributed. The R on the same horizontal line is only related to v and its direction is the same as v .

Liu et al. (Ref 25) explored the growth of long dendrites in the vertical plane of the cladding by the columnar to equiaxed transition (CET) model and found that the CET line can separate columnar and equiaxed grains in the normal direction. Therefore, the central cross-section of each cladding layer was selected as a reference to explore the variation of the G/R of the cladding layer in the z -axis direction (the sampling points are shown in Fig. 6a and b). Increasing equiaxed crystals and grain refinement help to reduce the tendency to crystalline cracking and enhance the strength and toughness of the material (Ref 26). Therefore, G/R should be selected to ensure the quality of the cladding and to improve the performance of the coating. Calculate the average G/R in the perpendicular direction of the center section of the 1-3 cladding with the results of groups 1-9 as 25.19, 58.80, 250.34, 31.96, 91.61, 63.60, 45.18, 30.30, and 92.05, respectively. Among them, the G/R of groups 3, 5, and 9

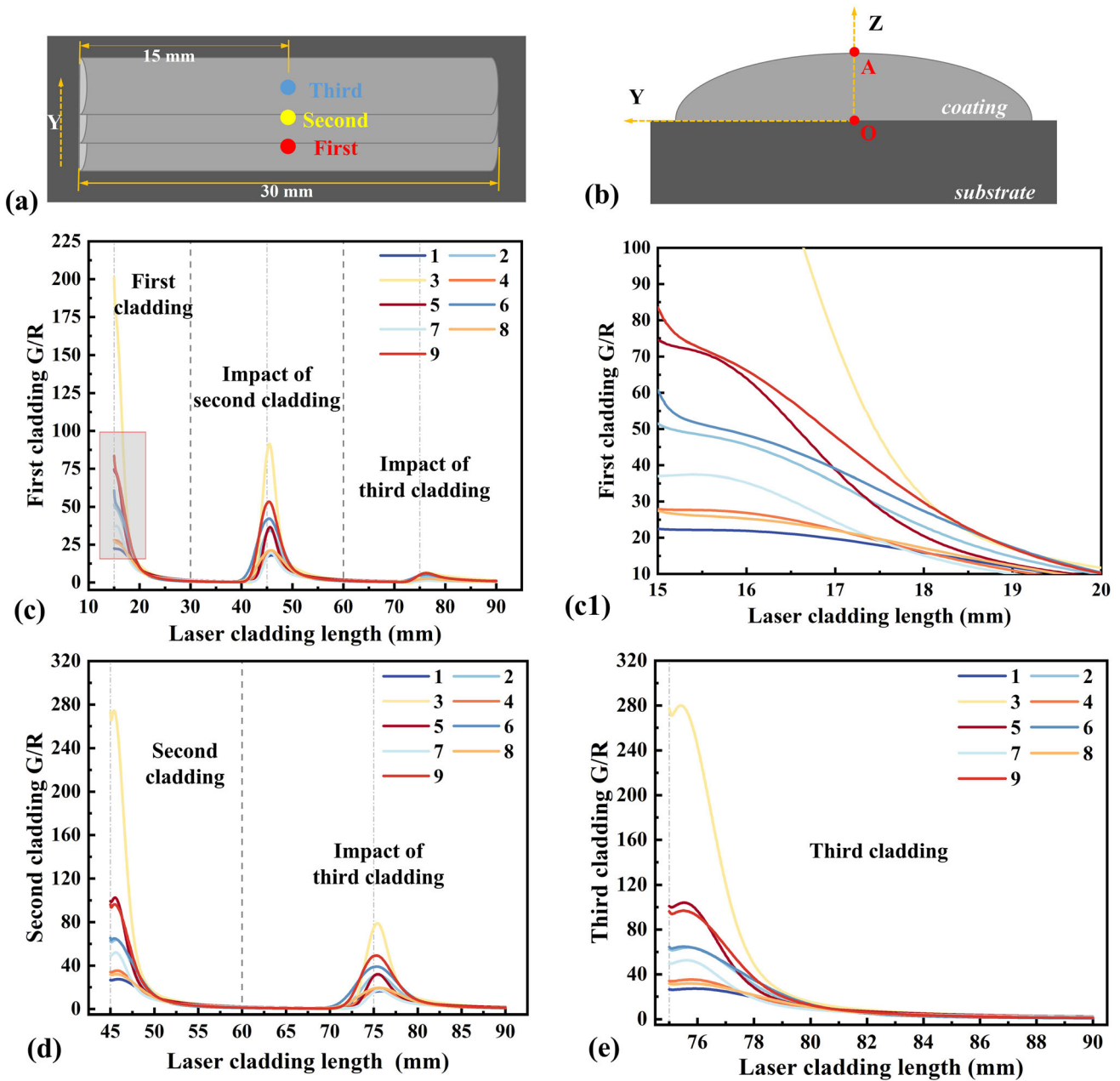


Fig. 6 (a-b) Schematic diagram of selected points of coating section; the coating G/R curves: (c) first, (d) second, (e) third

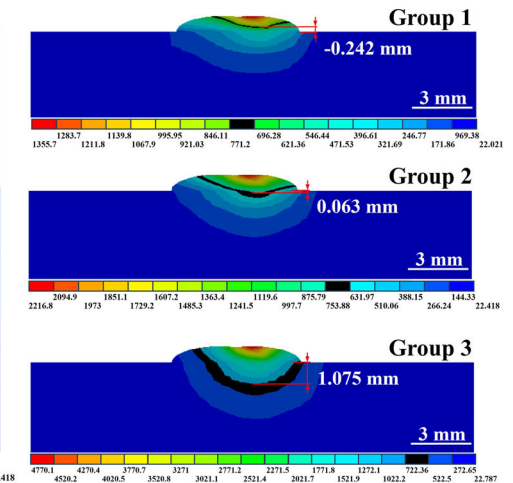
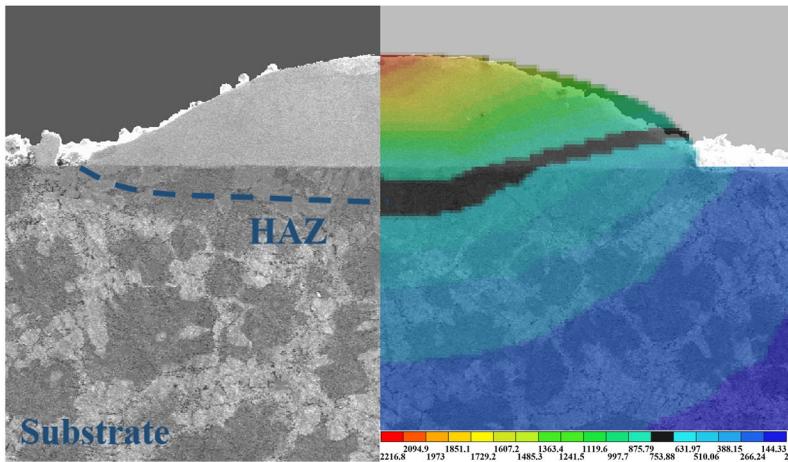
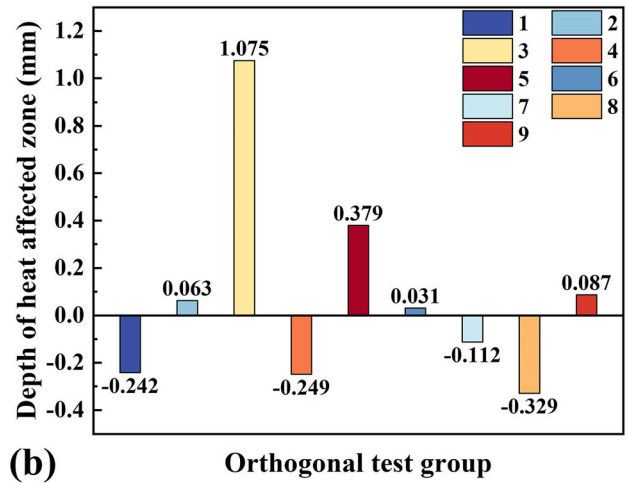
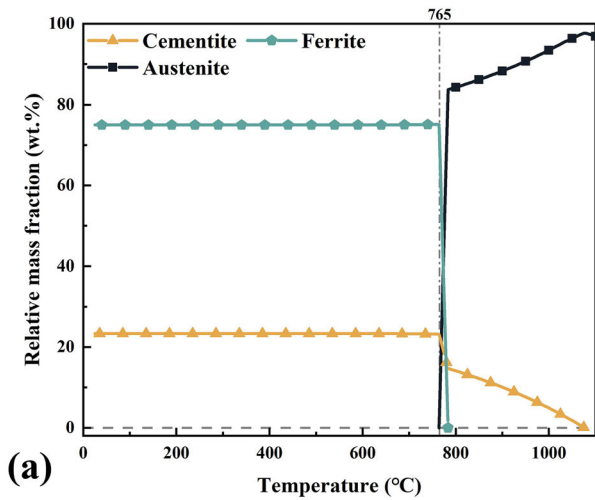


Fig. 7 (a) Phase change curve of gray cast iron, (b) PTZ depth of the middle of the second cladding in Groups 1-9, (c) comparison of HAZ for Group 2, (d) HAZ for groups 1-3

($r = 2$ mm or $v = 15$ mm/s) are too large, and their microstructure may consist of more long dendrites and columnar crystals, which will lead to a lack of coating properties.

3.4 PTZ

From Fig. 7(a), it can be seen that the substrate phase undergoes a significant phase change at 765 °C, with an increase in austenite and a decrease in the proportion of ferrite and cementite. Therefore, 765 °C was chosen as the temperature of the substrate phase transition, and the black contour line at 765 °C (± 15 °C) was used as the measurement range of the PTZ. Figure 7(b) shows the PTZ depth for each group. Negative values appear in them to ensure the numerical validity of the orthogonal test results, and these negative values should be 0 in the actual experiments. Figure 7(c) is a comparison of experimental and simulated HAZ, and it can be found that the PTZ of simulated test Group 2 is similar to its real experimental results. Figure 7(d) shows the HAZ range and PTZ depth measurements for groups 1-3.

Liu et al. (Ref 27) found the presence of martensite in the HAZ in laser fusion cladding of gray cast iron surfaces, and its density is greater around graphite tissue. However, martensite

formation expands to cause phase change stresses, and in addition the coating exerts upward tensile stresses on the substrate, which in combination cause the substrate to crack and warp (Ref 28). Therefore, during laser cladding of cast iron, the formation of martensite and brittle layer at the bonding interface will affect the bonding quality. On the other hand, Xi et al. (Ref 29) found that HAZ has a certain relationship with the depth of the molten pool and the dilution rate, and higher or lower dilution rates are detrimental to the quality of the cladding and the bond strength of laser cladding. In summary, groups 3 and 5 ($r = 2$ mm or $v = 15$ mm/s) had larger PTZ depths, which could lead to substrate warpage. The PTZ was not found (i.e., the PTZ values were negative) in the substrates of groups 1, 4, 7, and 8 ($r = 4$ mm or $v = 45$ mm/s), and the lower depth of the melt pool reduces the bonding strength between the coating and substrate.

3.5 Orthogonal Test Analysis

Based on the above analysis results, the degree of influence of P , v and r on the cladding quality was explored by taking the substrate surface temperature, G/R and PTZ depth as the analysis indexes. According to the orthogonal test analysis

Table 3 Numerical analysis results of orthogonal tests

	P	v	r
\bar{T}_1	1026.83	577.57	532.20
\bar{T}_2	783.67	770.00	737.73
\bar{T}_3	629.77	1092.70	1170.33
R_T	397.07	515.13	638.13
$(\bar{G}/R)_1$	111.44	34.11	39.70
$(\bar{G}/R)_2$	62.39	60.24	60.94
$(\bar{G}/R)_3$	55.84	135.33	129.04
$R_{G/R}$	55.60	101.22	89.35
\bar{D}_1	0.299	- 0.201	- 0.180
\bar{D}_2	0.054	0.038	- 0.033
\bar{D}_3	- 0.118	0.398	0.447
R_D	0.417	0.599	0.627

method, the corresponding mean and extreme differences were calculated, and the results are shown in Table 3.

The \bar{T} in Table 3 indicates the temperature value corresponding to the value of this parameter in addition to the rest of the parameters. Similarly, (\bar{G}/R) and \bar{D} correspond to the G/R value and PTZ depth, respectively. The R_T , $R_{G/R}$, and R_D denote the extreme values of temperature, G/R , and PTZ depth, respectively, and can be used to determine the extent to which the three parameters affect the factor. As seen in Table 3, the order of influence of each process parameter on T , G/R , and PTZ depth during Ni-based coating cladding is $r > v > P$, $v > r > P$, and $r > v > P$. Therefore, the process parameters that have the most significant effect on the coating cladding quality and the metallurgical bond's strength are v and r . Selecting the appropriate v and r will prevent cracking and warping of the substrate while ensuring bond strength and coating performance (Ref 30, 31).

In conclusion, $r = 2/4$ mm and $v = 15/45$ mm/s are not favorable for practical experiments and coating quality. Therefore, in order to ensure the Ni-based coating quality, bonding strength, and high processing efficiency. The combination of $v = 30$ mm/s and $r = 3$ mm was selected as the process parameters for the subsequent Ni-based coating cladding experiments.

4. Results and Discussion

To further optimize P , cladding experiments were performed on gray cast iron at $P = 1600, 2000$ and 2400 W. At $v = 30$ mm/s and $r = 3$ mm, there was no warping or cracking of the substrate; metallurgical bonding was good; no defects such as porosity were observed in the coating.

4.1 Microstructure

Figure 8(a), (b) and (c) show the degree of influence of process parameters on the results of orthogonal tests. It reflects the positive or inverse relationship between the process parameters and the three factors. Figure 8(d), (e) and (f) show the SEM microstructure morphology of the cladding layer. Compared with the 1600 W microstructure in Fig. 8(d), there are more columnar crystals at 2000 W in Fig. 8(b). The 2400 W microstructure in Fig. 8(f) was more sparse, larger tissue size

and more significant long dendrites. The average dendrite size can be derived by calculating the dendrite area from the intercrystalline and intragranular color differences in Fig. 8(d) and (e) using the Weka plug-in for ImageJ software. The average size was 5.518, 7.494, and 11.851 μm^2 as measured by ImageJ software for the dendrite in Fig. 8(d), (e) and (f). Taking the average dendrite size of the 1600 W sample as a reference, the increase in P from 1600 to 2000 W is 35.41%, and for $P = 2400$ W, the increase is 114.77%. The growth rate of dendrite size in the experiment is consistent with the pattern of the effect of P on G/R (microstructure size) in Fig. 8(b), where the growth rate of dendrite size increases with increasing P .

The Ni-based coating in Fig. 8(d) was composed of a dark γ -Ni solid solution and a bright eutectic structure. The eutectic organization is mainly composed of phases such as Ni_3B , Ni_2Si , and Cr_{23}C_6 ; the incipient solid-solution phase is dominated by (PDF#87-0712); the γ -Ni belonged to the Fm-3 m space group and three diffraction peaks corresponded to the (111), (200), and (220) crystalline planes (Ref 32). Differences in elemental melting points cause high melting point components to crystallize first to form intercrystalline and low melting point components to crystallize later to form intragranular (Ref 33). The Ni, B, and C elements are significantly segregated, while non-metallic elements B and C tend to be enriched and precipitate between the dendrites. Wei et al. (Ref 34) found that Fe, Ni, and Si were higher in intercrystalline than intragranular, which is consistent with the results obtained in Fig. 8(g).

Figure 8(h) shows the tissue size scatter plot, and combined with Fig. 8(d), (e) and (f), it was found that the size distribution of 1600 W is concentrated and the microstructure of the cladding layer is more dense and uniform. Fig. 8(i) shows the larger diameter size of the three experiments of samples, corresponding to the dendrites colored in Fig. 8(d), (e) and (f). It can be seen that there are large differences in 2400 W dendrite size, and 2000 W dendrite size fluctuates less. According to Eq 6, increasing the P enhances the thermal flow density and G/R value when the v is constant. The higher laser energy provides higher thermal energy, which prolongs the grain growth time and makes the grains transform into larger dendrites and columnar crystals (Ref 35, 36). The results of SEM and planar crystal measurements are consistent with the pattern obtained from the orthogonal test. Lv et al. (Ref 37) also found that the columnar crystal volume fraction increased with increasing P .

4.2 Hardness Distribution

Figure 9 shows the microhardness distribution of the cross-section of the cladding layer, the hardness of the cladding layer is obviously higher than that of the substrate, and the microhardness of the cladding layer increases slightly with the increase of P . The simulation experiments showed that raising P increases the heat-affected zone, melt pool depth and dilution rate. The dilution rate has a large effect on the hardness of the lower part of the cladding layer, and its hardness trend is inversely proportional to P (Ref 38). The average microhardness of 1600 W, 2000 W and 2400 W coating sections were 421.49, 429.21 and 433.05 $\text{HV}_{0.2}$, which is about 1.5-1.6 times higher than the average microhardness of the substrate (167.98 $\text{HV}_{0.2}$). The surface hardness of the coating is 42.56, 43.59 and 44.22 HRC in order with the raising of P . The change of surface hardness and cross-sectional hardness was minor.

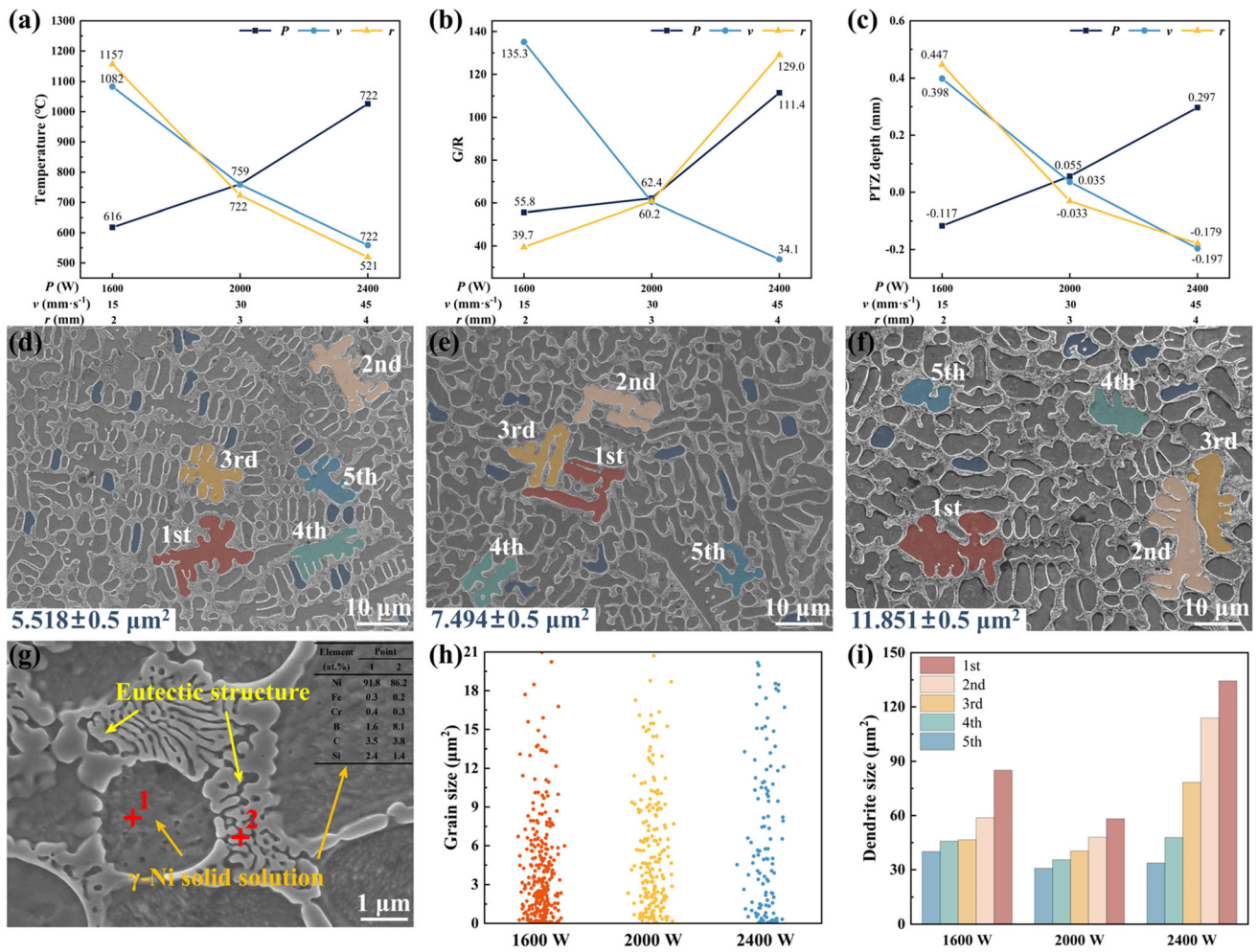


Fig. 8 (a-c) Relationship between process parameters and factors; SEM of the coating: (d) 1600 W, (e) 2000 W, (f) 2400 W, (g) 15000 times; (h) organization size distribution; (i) branch crystal size

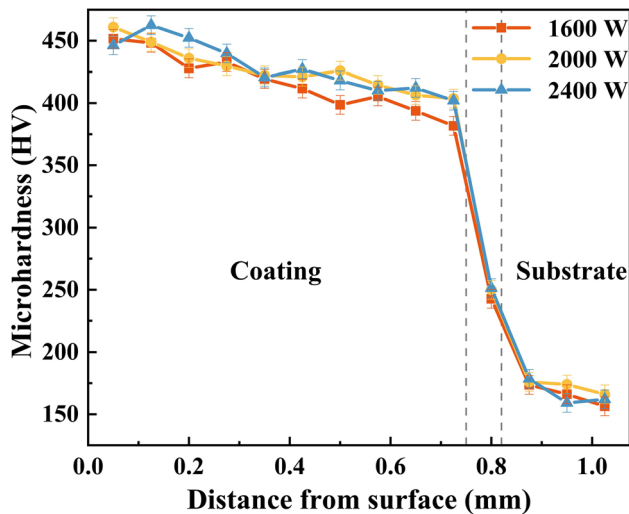


Fig. 9 Microhardness of the coating section

4.3 Frictional Wear

Figure 10(a) shows the friction coefficient curves for different parameters of P , and the average friction coefficients are 0.763, 0.550, and 0.791 for 1600 W, 2000 W, and 2400 W. In the initial stage of wear, the frictional contact area was less and the friction coefficient increased sharply; as the frictional contact area increased, the friction coefficient tended to stabilize (Ref 39). The overall friction coefficient of 1600 W is more steady, while 2000 W has a slowly increasing friction coefficient in the first 5 min, and 2400 W has the minimum friction coefficient in the 5-10 min wear phase. At the later stage of wear (> 30 min), the friction ball contact area gradually reaches the maximum, and the friction coefficient appears to be significantly stratified, with the most stability of 2000 W fluctuation. From Fig. 10(b), the wear quality of each group is 3.12, 2.5, and 3.51 mg. The wear quality of the cladding layer and the average friction coefficient are consistent with each other, and they all increase with the rise of P .

Measure the dimensions of the abrasion marks by using the surface profilometer, which is showed in Fig. 11, and combine

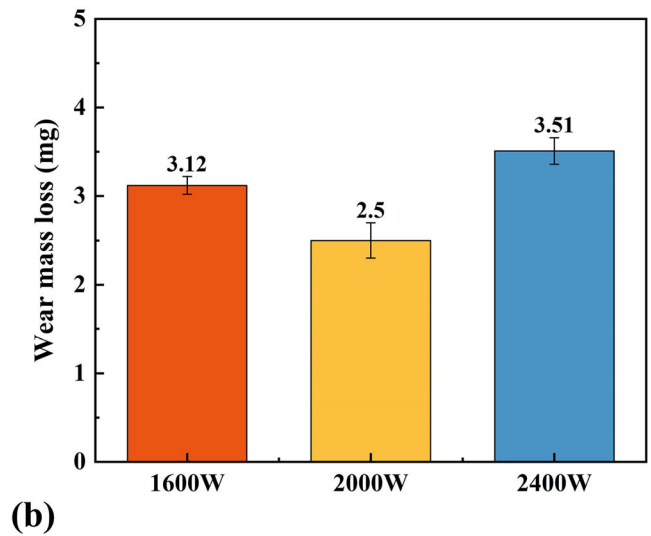
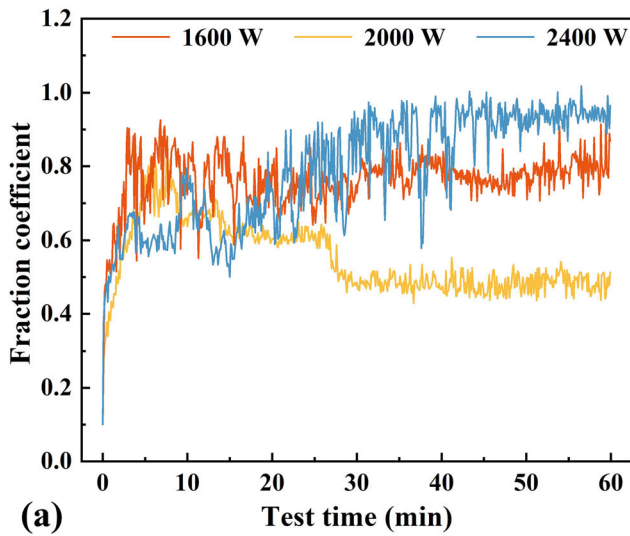


Fig. 10 Frictional wear of the coating: (a) friction coefficient; (b) wear quality

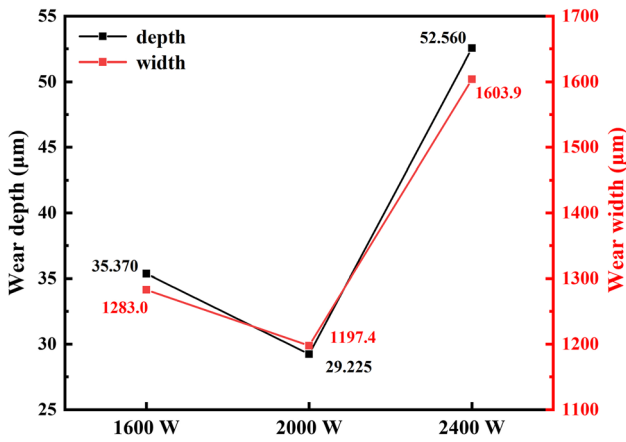


Fig. 11 Coating wear size

with the shape of the ultra-deep field abrasion marks in Fig. 12, and it can be seen that the width of the abrasion marks for the three P are 1283.0, 1197.4, and 1603.9 μm , and the depth of the abrasion marks are 35.37, 29.225, and 52.56 μm . The friction coefficient decreases with increasing hardness of the coating, but homogeneous and fine grains provide favorable wear resistance, while a higher number of long dendrites causes a reduction in wear performance (Ref 40). The coefficient of friction and wear quality of the 2000 W cladding layer was the lowest, and combination with the SEM and ultra-deep field images of the wear marks also showed more homogeneous wear. Therefore its wear resistance was superior to the other samples.

4.4 Wear Shape

Figure 13 shows the SEM of the coating wear marks. The main wear forms of the cladding layer are abrasive wear, oxidation wear and adhesion wear. During the friction process a few materials are squeezed by the Si_3N_4 ceramic balls to form bumps on both sides of the abrasion marks. The hard particles

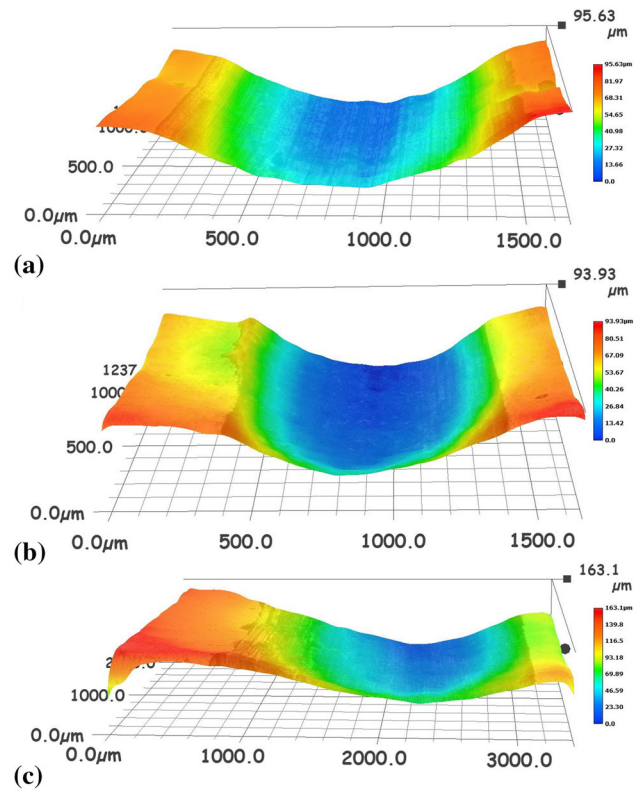


Fig. 12 3D abrasion profile of the coating: (a) 1600 W; (b) 2000 W; (c) 2400 W

dropped by friction adhere to the friction sub and the cladding layer and continue to squeeze the adjacent cladding layer tissue, and adhesive wear occurs to intensify the coating wear (Ref 41). 1600 W has significant flake exfoliation and irregular shape of the edge of the abrasion marks. 2000 W was severely oxidized and more scratches parallel to the direction of reciprocal friction were found at the bottom of 2400 W abrasions. Exfoliation, debris, scratches and wear oxidation

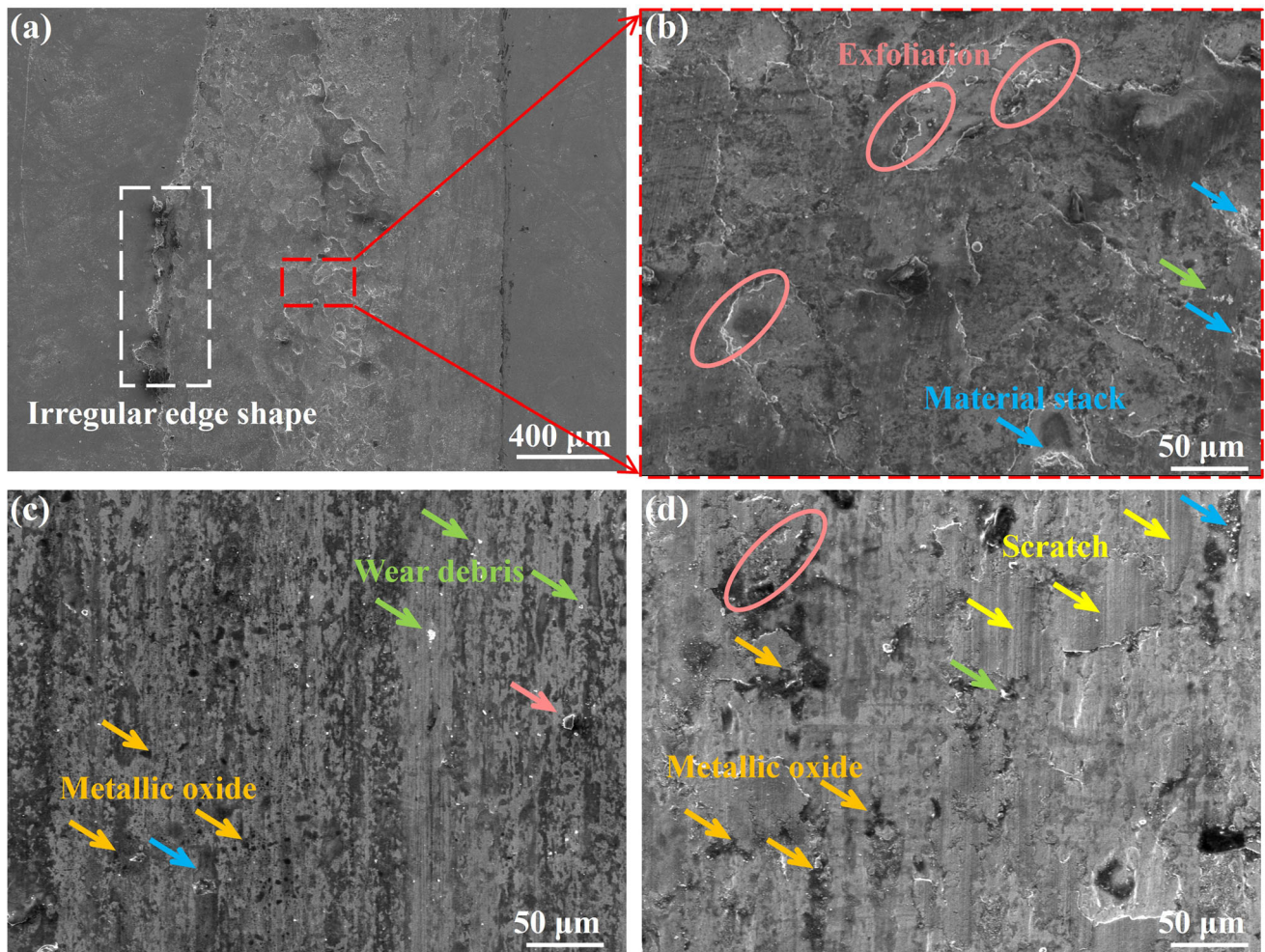


Fig. 13 Wear morphology SEM of coating: (a–b) 1600 W; (c) 2000 W; (d) 2400 W

were found at the bottom of all three coating abrasions, with material delamination clearly observed at 1600 and 2400 W.

Figure 14 shows the 2000 W melt layer wear marks EDS. Combining the atomic number percentages of each element shows that the black area point 3 has significantly more O elements compared to the white scratched area marking points 1 and 2 (Fig. 14b). From Fig. 14(c), it can be observed that Ni, Si, and Cr elements are evenly distributed, and there is a certain segregation of O elements especially in the black area corresponding to Fig. 14(b). abrasion induced oxide (Cr_2O_3 , Fe_3O_4 , NiO) formation and exfoliation (show Fig. 13a and b), and all coatings suffered plastic deformation. Pereira et al. (Ref 42) also found similar oxides and coating plastic deformation during friction of MCrAlY cladding layers.

5. Conclusion

The analytical model of temperature field of laser cladding Ni-based powder of gray cast iron was established by using ANSYS simulation software. The effect of r , v and P on the cladding quality was explored by analyzing the temperature distribution, G/R, and PTZ depth in a three-factor and three-level orthogonal test. The microstructure and wear resistance of

coatings for different P were analyzed. The research results are as follows:

- (1) Those are in good agreement with the numerical results and verify the validity of the model, which are consistent with the numerical simulation. In the cladding process, the effect factors on the T and PTZ depth are r , v and P . The v and r most significantly affects the microstructure, and the P has less effect on it. The combination of process parameters of $r = 3$ mm and $v = 30$ mm/s has good laser cladding results.
- (2) The Ni-based coating consists of γ -Ni solid solution and eutectic structure. The average plane crystal size of the three P groups is 5.518, 7.494, and 11.851 μm^2 , and the plane crystal size increases with the increase of P . The microstructure is more uniform and fine-grained at 1600 W. The microstructure is sparse and the long dendrites are significant at 2400 W.
- (3) With the increase of P , the hardness of the cladding layer is not changed much, the average friction coefficient is raised and the wear resistance is decreased. The average coefficient of friction of the 2400 W cladding (0.791) is almost the same as 1600 W (0.763), and the minimum is 2000 W (0.550). The wear quality of 2000

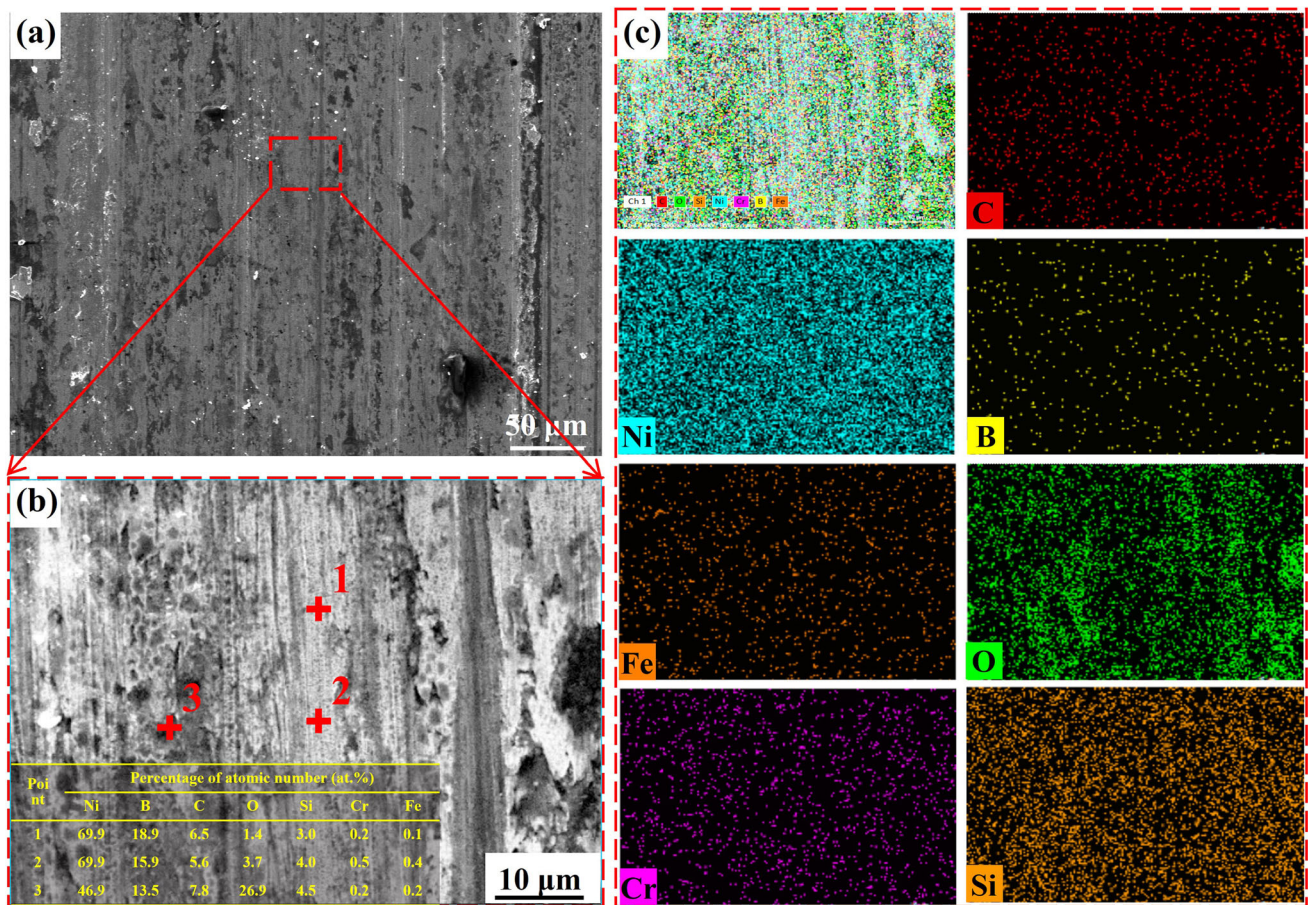


Fig. 14 (a) 2000 W coating; (b–c) EDS of partial enlarged detail

W (2.5 mg) is only 71.2% of 2400 W (3.51 mg), so the wear resistance of the 2000 W coating is the best.

Conflict of interest

The authors declare that they have no conflict of interest.

Author Contributions

All authors contributed to the study conception and design. Material preparation, data collection and analysis were performed by RW, MM, CO, RW and CZ. The first draft of the manuscript was written by HL and all authors commented on previous versions of the manuscript. All authors read and approved the final manuscript.

Funding

This research was supported financially by the National Natural Science Foundation of China (No. 52275358) and University Doctoral Research Initiation Grant (No. 2023085).

Data Availability

The datasets generated during and/or analyzed during the current study are available from the corresponding authors upon reasonable request.

References

1. A. Adedayo, Characterization of Graphite Flakes in gray Iron Microstructure, *Arab. J. Sci. Eng.*, 2012, **37**, p 1645–1652. (in English)
2. G. Wang, Z. Liu, Y. Li, and X. Chen, Different Thermal Fatigue Behaviors Between Gray Cast Iron and Vermicular Graphite Cast Iron, *China Foundry*, 2022, **19**, p 245–252. (in English)
3. S. Fischer, S. Muschna, A. Buhrig-Polaczek, and M. Bunck, In-Situ Surface Hardening of Cast Iron by Surface Layer Metallurgy, *Mat. Sci. Eng. A-Struct.*, 2014, **615**, p 61–69. (in English)
4. A. Sadeghi, A. Moloodi, M. Golestanipour, and M. Shahrri, An Investigation of Abrasive Wear and Corrosion Behavior of Surface Repair of Gray Cast Iron by SMAW, *J. Mater. Res. Technol.*, 2017, **6**, p 90–95. (in English)
5. H. Li, L. Feng, H. Zhou, P. Zhang, T. Zhou, Q. Sui, and L. Ren, Influence of Varying Forms of Bionic Units on Repairing Remaining Quenching Surface of Gray Cast Iron, *J. Iron. Steel Res. Int.*, 2021, **28**, p 201–210. (in English)
6. A. Siddiqui and A. Dubey, Recent Trends in Laser Cladding and Surface Alloying, *Opt. Laser Technol.*, 2021, **134**, p 106619. (in English)
7. L. Zhu, P. Xue, Q. Lan, G. Meng, Y. Ren, Z. Yang, P. Xu, and Z. Liu, Recent Research and Development Status of Laser Cladding: A Review, *Opt. Laser Technol.*, 2021, **138**, p 1006915. (in English)
8. L. Zhu, Y. Liu, Z. Li, L. Zhou, Y. Li, and A. Xiong, Microstructure and Properties of Cu-Ti-Ni Composite Coatings on Gray Cast Iron

- Fabricated by Laser Cladding, *Opt. Laser Technol.*, 2020, **122**, p 105879. **(in English)**
9. J. Ding, Y. Liu, L. Zhu, L. Zhou, and Y. Li, Microstructure and Properties of a Titanium Carbide Reinforced Coating on gray Iron Applied with Laser Cladding, *Mater. Tehnol.*, 2019, **53**(3), p 377–381. **(in English)**
 10. M. Kiehl, A. Scheid, K. Graf, B. Ernst, and U. Tetzlaff, Coaxial Laser Cladding of Cobalt-Base Alloy Stellite™ 6 on Gray Cast Iron/ Investigations on Friction, Wear Versus Commercial Brake Pad, and Corrosion Characteristics, *P. I. Mech. Eng. D-J. Aut.*, 2023, **237**, p 3285–3303. **(in English)**
 11. T. Yu, L. Yang, Y. Zhao, J. Sun, and B. Li, Experimental Research and Multi-Response Multi-Parameter Optimization of Laser Cladding Fe313, *Opt. Laser Technol.*, 2018, **108**, p 321–332. **(in English)**
 12. J. Kim and Y. Peng, Melt Pool Shape and Dilution of Laser Cladding with Wire Feeding, *J. Mater. Process Tech.*, 2000, **104**, p 284–293. **(in English)**
 13. H. Tian, X. Chen, Z. Yan, X. Zhi, Q. Yang, and Z. Yuan, Finite-Element Simulation of Melt Pool Geometry and Dilution Ratio During Laser Cladding, *Appl. Phys. A-Mate.*, 2019, **125**, p 1–9. **(in English)**
 14. P. Yi, X. Zhan, Q. He, Y. Liu, P. Xu, P. Xiao, and D. Jia, Influence of Laser Parameters on Graphite Morphology in the Bonding Zone and Process Optimization in Gray Cast Iron Laser Cladding, *Opt. Laser Technol.*, 2019, **109**, p 480–487. **(in English)**
 15. F. Huang, Z. Jiang, X. Liu, J. Lian, and L. Chen, Effects of Process Parameters on Microstructure and Hardness of Layers by Laser Cladding, *ISIJ int.*, 2011, **51**, p 441–447. **(in English)**
 16. D. Goodarzi, J. Pekkarinen, and A. Salminen, Effect of Process Parameters in Laser Cladding on Substrate Melted Areas and the Substrate Melted Shape, *J. Laser Appl.*, 2015 <https://doi.org/10.2351/1.4906376>. **(in English)**
 17. P. Nie, O. Ojo, and Z. Li, Modeling Analysis of Laser Cladding of a Nickel-Based Superalloy, *Surf. Coat. Tech.*, 2014, **258**, p 1048–1059. **(in English)**
 18. P. Ma, Y. Wu, P. Zhang, and J. Chen, Solidification Prediction of Laser Cladding 316L by the Finite Element Simulation, *Int. J. Adv. Manuf. Tech.*, 2019, **103**, p 957–969. **(in English)**
 19. H. Liu, M. Li, X. Qin, S. Huang, and F. Hong, Numerical Simulation and Experimental Analysis of Wide-Beam Laser Cladding, *Int. J. Adv. Manuf. Tech.*, 2019, **100**, p 237–249. **(in English)**
 20. Q. Bai, C. Ouyang, C. Zhao, B. Han, and Y. Liu, Microstructure and Wear Resistance of Laser Cladding of Fe-Based Alloy Coatings in Different Areas of Cladding Layer, *Materials*, 2021, **14**, p 2839. **(in English)**
 21. Y. Javid and M. Ghoreishi, Thermo-Mechanical Analysis in Pulsed Laser Cladding of WC Powder on INCONEL 718, *Int. J. Adv. Manuf. Tech.*, 2017, **92**, p 69–79. **(in English)**
 22. J. Yin, H. Zhu, L. Ke, P. Hu, C. He, H. Zhang, and X. Zeng, A Finite Element Model of Thermal Evolution in Laser Micro Sintering, *Int. J. Adv. Manuf. Tech.*, 2016, **83**, p 1847–1859. **(in English)**
 23. R. Wei, C. Ouyang, R. Wang, C. Zhao, H. Li, and R. Deng, Research Status of the Transition Layer on Laser Cladding, *Metall. Res. Technol.*, 2023, **120**, p 318. **(in English)**
 24. Y. Cheng, C. Cao, X. Yang, J. Zhou, J. Yang, X. Liang, and X. Li, Effects of Laser Energy Density and Path on Residual Stress of Remanufactured Key Components for Shield Tunneling Machine, *Mater. Chem. Phys.*, 2022, **290**, p 126617. **(in English)**
 25. S. Liu, H. Zhu, G. Peng, J. Yin and, X. Zeng, Microstructure Prediction of Selective Laser Melting als10 mg Using Finite Element Analysis, *Mater. Design*, 2018, **142**, p 319–328. **(in English)**
 26. Y. Shi, X. Zhou, X. Wang, X. Feng, and L. Peng, Effects of Electromagnetic Fields on the Microstructure of Laser Cladding, *Materials*, 2022, **15**, p 4198. **(in English)**
 27. Y. Liu, X. Zhan, P. Yi, T. Liu, B. Liu, and Q. Wu, Research on the Transformation Mechanism of Graphite Phase and Microstructure in the Heated Region of Gray Cast Iron by Laser Cladding, *Opt. Laser Technol.*, 2018, **100**, p 79–86. **(in English)**
 28. H. Liu, J. Hao, Z. Han, G. Yu, X. He, and H. Yang, Microstructural Evolution and Bonding Characteristic in Multi-Layer Laser Cladding of Nicocr Alloy on Compacted Graphite Cast Iron, *J. Mater. Process. Tech.*, 2016, **232**, p 153–164. **(in English)**
 29. W. Xi, B. Song, Y. Zhao, T. Yu, and J. Wang, Geometry and Dilution Rate Analysis and Prediction of Laser Cladding, *Int. J. Adv. Manuf. Tech.*, 2019, **103**, p 4695–4702. **(in English)**
 30. J. Yang, B. Bai, H. Ke, Z. Cui, Z. Liu, Z. Zhou, H. Xu, J. Xiao, Q. Liu, and H. Li, Effect of Metallurgical Behavior on Microstructure and Properties of FeCrMoMn Coatings Prepared by High-Speed Laser Cladding, *Opt. Laser Technol.*, 2021, **144**, p 107431. **(in English)**
 31. D. Wang, Q. Hu, Y. Zheng, Y. Xie, and X. Zeng, Study on Deposition Rate and Laser Energy Efficiency of Laser-Induction Hybrid Cladding, *Opt. Laser Technol.*, 2016, **77**, p 16–22. **(in English)**
 32. R. Wang, C. Ouyang, Q. Li, Q. Bai, C. Zhao, and Y. Liu, Microstructure and Corrosion Properties of a Ni-Based Alloy Coating Deposited onto the Surface of Ductile Cast Iron Using High-Speed Laser Cladding, *Materials*, 2022, **15**, p 1643. **(in English)**
 33. J. Zhang, C. Zhao, Q. Bai, Q. Li, C. Chen, and J. Liang, Effect of Ultrasonic High-Frequency Percussion on the Microstructure and Corrosion Resistance of Fe-Based Alloy Coatings by High-Speed Laser Cladding, *Mater. Lett.*, 2023, **335**, p 133769. **(in English)**
 34. R. Wei, C. Ouyang, R. Wang, C. Zhao, R. Deng, and H. Li, Effect of Chromic Acid Anodization on the Corrosion Resistance of Fe-Based Alloy Coatings by High-Speed Laser Cladding, *Mater. Lett.*, 2023, **350**, p 134887. **(in English)**
 35. J. Pekkarinen, A. Salminen, and V. Kujanpaa, Laser Cladding with Scanning Optics: Effect of Scanning Frequency and Laser Beam Power Density on Cladding Process, *J. Laser Appl.*, 2014, **26**, p 032002. **(in English)**
 36. M. Fesharaki, R. Shoja-Razavi, H. Mansouri, and H. Jamali, Microstructure Investigation of Inconel 625 Coating Obtained by Laser Cladding and TIG Cladding Methods, *Surf. Coat. Tech.*, 2018, **353**, p 25–31. **(in English)**
 37. H. Lv, X. Li, Z. Li, W. Wang, K. Yang, F. Li, and H. Xie, Investigation on the Columnar-to-Equiaxed Transition During Laser Cladding of IN718 alloy, *J. Manuf. Process.*, 2021, **67**, p 63–76. **(in English)**
 38. A. Khorram, Microstructural Evolution of Laser Clad Stellite 31 Powder on Inconel 713 LC superalloy, *Surf. Coat. Tech.*, 2021, **423**, p 127633. **(in English)**
 39. Y. Zhao, T. Yu, C. Guan, J. Sun, and X. Tan, Microstructure and Friction Coefficient of Ceramic (TiC, TiN and B4C) Reinforced Ni-Based Coating by Laser Cladding, *Ceram. Int.*, 2019, **45**, p 20824–20836. **(in English)**
 40. S. Qian, Y. Dai, Y. Guo, and Y. Zhang, Microstructure and Wear Resistance of Multi-Layer Ni-Based Alloy Cladding Coating on 316L SS Under Different Laser Power, *Materials*, 2021, **14**, p 781. **(in English)**
 41. W. Li and D. Kong, Effects of TiO2 Mass Fraction on Friction Reduction and Wear Resistance of Laser-Cladded CrNi, *J. Mater. Eng. Perform.*, 2021, **30**, p 2280–2290. **(in English)**
 42. J. Pereiram, J. Zambrano, M. Licausi, M. Tobar, and V. Amigo, Tribology and High Temperature Friction Wear Behavior of MCrAlY Laser Cladding Coatings on Stainless Steel, *Wear*, 2015, **330**, p 280–287. **(in English)**

Publisher's Note Springer Nature remains neutral with regard to jurisdictional claims in published maps and institutional affiliations.

Springer Nature or its licensor (e.g. a society or other partner) holds exclusive rights to this article under a publishing agreement with the author(s) or other rightsholder(s); author self-archiving of the accepted manuscript version of this article is solely governed by the terms of such publishing agreement and applicable law.